1.3 μm emitting $SrF_2:Nd^{3+}$ nanoparticles for high contrast *in vivo* imaging in the second biological window.

Irene Villa,[†] Anna Vedda, [†] Irene Xochilt Cantarelli,[˚] Marco Pedroni, [˚] Fabio Piccinelli, [˚] Marco Bettinelli, [˚] Adolfo Speghini, [˚] Marta Quintanilla,[∞] Fiorenzo Vetrone, [∞] Ueslen Rocha,[‡] Carlos Jacinto, [‡] Elisa Carrasco,[§] Francisco Sanz Rodríguez, [§] Ángeles Juarranz de la Cruz, [§] Blanca del Rosal,[□] Dirk H. Ortgies,[□] Patricia Haro Gonzalez,[□] José García Solé, [□] and Daniel Jaque García.[□]*

[†] Department of Materials Science, University of Milano-Bicocca, Via R. Cozzi 55 , 20125 Milano, Italy, [˚] Dipartimento di Biotecnologie, Università di Verona and INSTM, UdR Verona, Strada le Grazie 15, 37134, Verona, Italy, [∞] Institut National de la Recherche Scientifique-Energie Materiaux et Telecommunications, Université du Quebec, Varennes, QC, PQ J3X 1S2, Canada, [‡] Grupo de Fotônica e Fluidos Complexos, Instituto de Física, Universidade Federal de Alagoas, 57072-970, Maceió, Alagoas, Brazil, [§] Departamento de Biología, Facultad de Ciencias, Campus de Cantoblanco, Universidad Autónoma de Madrid, Madrid, 28049, Spain, [□] Fluorescence Imaging Group, Departamento de Física de Materiales, Facultad de Ciencias, Campus de Cantoblanco, Universidad Autónoma de Madrid, Madrid, 28049, Spain.

ABSTRACT.- Novel approaches for high contrast, deep tissue, *in vivo* fluorescence biomedical imaging are based on infrared-emitting nanoparticles working in the so-called second biological window (1000 -1400 nm). This allows for the acquisition of high resolution, deep tissue images due to the partial transparency of tissues in this particular spectral range. In addition, the optical excitation with low energy (infrared) photons also leads to a drastic reduction in the contribution of autofluorescence to the *in vivo* image. Nevertheless, as it is here demonstrated, working solely in this biological window does not ensure a complete removal of autofluorescence as the specimen's diet shows a remarkable infrared fluorescence that extends up to 1100 nm. In this work, we show how the 1340 nm emission band of Nd^{3+} ions embedded in SrF_2 nanoparticles can be used to produce auto-fluorescence free, high contrast in vivo fluorescence images. It is also demonstrated that the complete removal of the food-related infrared autofluorescence is imperative for the development of reliable bio-distribution studies.

KEYWORDS; Fluorescence Imaging, Rare earth doped nanoparticles, Nanomedicine,

1.-INTRODUCTION

Nanotechnology has catalyzed a revolution in the area of biomedicine, leading to the appearance of new materials and techniques for the improvement of detection, imaging, diagnosis and therapy procedures.[1-7] In particular, a great scientific effort has been undertaken on the design, synthesis, characterization, and application of nanometer-size particles (nanoparticles, NPs) that can function as biomarkers, biosensors and, even, as therapeutic agents.[8-13] In particular, much attention has been paid to the development of luminescent nanoparticles (LNPs) for bioimaging applications.[14-18] The optimization of the synthesis procedures has made possible the production of LNPs with specifically engineered and tailored properties. This is the case, for instance, of semiconductor quantum dots (QDs) or rare earth doped nanoparticles (RENPs) in which the spectral working range can be controlled by an adequate selection of synthesis conditions or of the doping fluorescent ions for QDs and RENPs, respectively. In addition, chemical methods have evolved such that a fine tuning of the LNPs surface coating is now possible.[19-21] This has been vital for the production of colloidal solutions of LNPs dispersed in biocompatible liquids, thus allowing for their direct injection in the blood stream for *in vivo* bioimaging experiments. Surface coating treatments have been also employed to endow LNPs with specific affinity by linking them with tumour targeting ligands such as monoclonal antibodies, peptides, or small molecules.[8] As a result of all these and many other key advancements in the field, LNPs are currently being considered as buiding block for real *in vivo* tumor detection at early stages, which would lead to a substantial increment in the treatment efficacy.[22] Despite the great advances already achieved in the use of LNPs as bioimaging agents,[23, 24] their use for real *in vivo* fluorescence imaging and detection of incipient tumors is restricted because of both the tissue-induced optical attenuation and autofluorescence.[25, 26] Light attenuation (extinction) in living specimens is caused by the interplay between the tissue light scattering and the optical

absorptions of the different biological media (water, blood, haemoglobin, melanin and lipids).[25] Indeed, the extinction coefficient of tissues and living specimens ($\alpha_{ext.}$) is usually written as the sum of the scattering coefficient ($\alpha_{sct.}$) and the absorption coefficient ($\alpha_{abs.}$), in such a way that: $\alpha_{ext.} = \alpha_{sct.} + \alpha_{abs.}$.[27] During *in vivo* fluorescence imaging experiments, light must propagate in a complex inhomogeneous medium (different tissues) and so extinction leads to a reduced intra-body penetration length of both excitation and fluorescence radiations. This, in turns, inhibits imaging of deep tissues features, for instance, intra-body (non-superficial) tumors. As stated above, fluorescence imaging for *in vivo* applications is not only limited by light attenuation but also by the presence of autofluorescence, i.e. the fluorescence generated by tissues and intra-body components.[28] Autofluorescence leads to the appearance of an undesirable background signal during *in vivo* fluorescence imaging experiments, reducing the brightness and contrast of the obtained images. In particular, the presence of this autofluorescence during LNP based *in vivo* imaging experiments makes the interpretation of the obtained images difficult and ambiguous as signal is also produced in tissues and organs where LNPs are not present. Thus, high-brightness, high contrast, and deep tissue *in vivo* imaging requires simultaneously overcoming both the light attenuation and autofluorescence. Indeed, this dual challenge has attracted a great deal of attention in the last few years. To date, one of the most suitable solutions proposed is the use of LNPs working in the so-called biological-windows (BWs), spectral regions in which tissues are partially transparent.[29] BWs are spectrally allocated in the infrared (>750 nm) since the use of long wavelengths reduces tissue-induced light scattering. Additionally, these windows correspond to spectral regions in which optical absorptions of tissues and inherent components (water, haemoglobin, lipids, food and so on) are minimized. Generally speaking there are three BWs; i) The first BW (I-BW) extending from 750 to 950 nm, which is limited by the visible absorption of hemoglobin and the 980 nm absorption band of water; ii) The

second BW (II-BW), extending from 1000 up to 1450 nm, is limited by the 980 and 1450 nm absorption bands of water; iii) The third BW (III-BW), that extends from 1500 up to 1700 nm, is sandwiched by two water absorption bands.[30, 31] A given LNP is said to work within BWs when both the excitation radiation and the generated emission lie within any of these three spectral ranges. This ensures that both excitation and fluorescence signals are weakly attenuated, resulting in a larger optical penetration and, thus, allowing for deeper imaging.[29] Minimization of the autofluorescence background, in turns, requires the use of excitation radiations that are not absorbed by tissues. Again, this implies the use of excitation sources working in any of the BWs since, as already stated, these spectral regions are characterized by a negligible optical absorption. It is, indeed, currently assumed that the use of excitation sources within any of the BWs would simultaneously lead to large penetration depths and to a complete removal of autofluorescence background. In this sense, infrared excitation sources and infrared imaging detection systems seem to constitute an unique and ideal combination for real deep tissue high contrast *in vivo* bioimaging. Indeed, this belief has heightened the use of the so-called up-converting nanoparticles (UCNPs) and infrared (excitation) to infrared (emission) nanoparticles (IR-IR-NPs) for *in vivo* imaging.[32-35] Another smart alternative to avoid autofluorescence is the use of LNP showing what is called persistent luminescence, i.e. capable of fluorescence generation without requiring any optical excitation source.[36-39] Nevertheless, although the use of non-absorbed infrared radiations has led to a drastic reduction in the tissue autofluorescence, it does not ensure the complete absence of background signal. In fact, recent works have pointed out that during in vivo imaging experiments under certain experimental conditions an infrared background signal could appear, leading to a reduction in the image quality and contrast.[40] At present time little is known about the origin and spectral extension of this infrared autofluorescence, this last being essential for an appropriate choice of an appropriate LNP with minimum spectral

overlapping with infrared autofluorescence. This problem is faced in this work, in which we have investigated in detail the spectral extension of the infrared *in vivo* autofluorescence. Based on these studies we have proposed the use of the 1.3 μm emission band of Neodymium doped SrF_2 nanoparticles for the obtention of high contrast, auto-fluorescence free in vivo infrared imaging.

2.-RESULTS AND DISCUSION

2.1.- Spectral properties of infrared in vivo autofluorescence

Figure 1 shows the infrared fluorescence image of a non-treated mouse (i.e. a mouse with no LNPs injected). In this case, the optical excitation was performed in the I-BW (808 nm) while infrared fluorescence image was obtained in the whole II-BW by recording the entire emitted fluorescence in the 900-1500 nm spectral range (detection range of conventional AsGaIn infrared cameras). As can be observed, even in the absence of tissue absorption (and hence of tissue fluorescence), an infrared autofluorescence background is still present. Infrared autofluorescence is mainly generated from the mouse abdomen, suggesting that it is related to residual food. This assumption is, indeed, supported by the results recently published by several groups who reported on the presence of visible fluorescence generated from both the abdominal and lumbar regions of living animals during *in vivo* imaging experiments.[26, 40, 41] The proposed assignment of the infrared autofluorescence to the residual food is further supported by the images included in Figures 1(d)-(e) that correspond to the optical and infrared fluorescence images of several dregs obtained from conventional fed mice as obtained under 808 nm laser excitation. Indeed, high concentrations of food residuals and components are expected to be present in dregs. As can be observed, dregs also showed and intense infrared autofluorescence and this fact reinforces the tentative assignment of the infrared fluorescence background to the presence of different food components.

The infrared fluorescence images of **Figure 1** suggest that, under 808 nm optical excitation, the fluorescence generated by the animal diet is not restricted to the visible spectral range but it also extends into the infrared one. This fact was corroborated by the infrared fluorescence images of a conventional food pellet included in **Figure 2**. Optical excitation was, again, performed in the I-BW (808 nm) but in this case the fluorescent images were obtained, by using different long-band pass filters, in different spectral ranges. When the fluorescent image of food pellet is built up by recording the 900-1500 nm luminescence, a clear (high brightness) image is obtained. The intensity of infrared fluorescence generated by food pellets decreases as the "cut-off" wavelength of image is shifted to the infrared. As a matter of fact, no fluorescence image was obtained when the image was built up by recording image in the 1200-1500 nm range. From the fluorescence images included in **Figure 2** it is possible to obtain the emission spectrum of the food pellet autofluorescence (details are given in the methods section). Results are included in **Figure 2**. As can be observed, food autofluorescence extends up to about 1100 nm. Infrared autofluorescence was found to exist in all the different diets available in our animal center. Nevertheless it is important to note here that both the fluorescence intensity and spatial distribution within the pellets were found to be strongly dependent on the particular pellet analyzed. Concerning the possible origin of this infrared luminescence it has to be said that previous works dealing with the visible autofluorescence of animal food correlated it with the presence of plant components (in particular with the presence of alfalfa in the food pellets). [40] Furthermore, Y. Inoue et al. demonstrated that when chlorophyll was completely removed from animal diet, then *in vivo* infrared images (in this work obtained in the 775-825 nm spectral range) were absolutely free from autofluorescence.[40] At this point, we claim that the infrared food fluorescence here reported (extending up to 1100 nm) is also generated by the presence of plant components, in particular by chlorophyll. This assumption is based on previous works published by A. A.

Krasnovsky et al. who reported on chlorophyll related fluorescence bands extending from 850 up to 1120 nm, in good agreement with the autofluorescence spectrum included in **Figure 2**. [42]

2.2.- Nd:SrF_2nanoparticles for autofluorescence-free imaging

Up to this point, it is clear that high contrast (autofluorescence free) infrared *in vivo* imaging requires the use of LNPs that show intense fluorescence in the 1100-1400 nm region following optical excitation in any of the BWs. It has been demonstrated that these conditions are satisfied by a limited number of LNPs, including single walled carbon nanotubes (SWCNTs) and Ag_2S quantum dots (Ag_2S-QDs). [43, 44] Indeed, these LNPs have already been used for real-time, autofluorescence free, deep tissue *in vivo* and *in vitro* fluorescence imaging. [43-49] Despite the excellent results obtained so far by using these infrared probes, the search for other LNPs with bright luminescence in the 1100-1400 nm range is still ongoing. Very recently infrared emitting rare earth doped nanoparticles (RENPs) have attracted great attention as reliable alternative to QDs and SWCNTs for infrared *in vivo* imaging.[32, 50-54] RENPs offer outstanding properties, such as high fluorescence quantum yields, absence of "aging" (time-induced fluorescence deterioration), long term chemical and physical stability, particle size independent fluorescence spectra, and low toxicity. [41, 55-58] *In vivo* imaging with RENPs at wavelengths longer than 1200 nm has been recently obtained by Naczynski et al., who reported on deep tissue *in vivo* imaging by using Er^{3+} doped $NaYF_4$ nanocrystals.[59] Nevertheless, Er^{3+} ion emission (at about 1.5 μm ot 1500 nm) overlaps partially with water absorption, in such a way that image depths could be limited.[29] Alternatively, Nd^{3+} ion doped nanoparticles (Nd:NPs) are quite interesting systems as they could possess close-to-unity luminescence quantum yields and well-defined emission bands matching both I and II-BWs,

and that can be efficiently excited by 808 nm (I-BW) radiation.[50, 53, 54, 60] The emission spectrum of Nd^{3+} (after 808 nm optical excitation) displays three emission bands centered at around 900, 1060 and 1340 nm corresponding to the $^4F_{3/2}\rightarrow{}^4I_{9/2}$, $^4F_{3/2}\rightarrow{}^4I_{11/2}$ and $^4F_{3/2}\rightarrow{}^4I_{13/2}$ intra 4*f* electronic transitions of this ion, respectively.[61] This can be clearly ascertained from **Figure 2**, where the emission spectrum of the SrF_2:Nd nanoparticles used in this work has been drawn. In previous works regarding the use of Nd:NPs for *in vivo* imaging, Nd^{3+} ions were used as sensitizers for other visible emitting RE ions or, alternatively, their 900 and 1060 nm bands were directly used for fluorescence contrast. [50, 54, 62] Nevertheless, from **Figure 2** it is clear that the use of these two bands does not ensure the complete removal of food autofluorescence. In fact, according to **Figure 2**, this would be only achieved if fluorescence images were recorded based on the 1340 nm fluorescence band. The principal reason explaining why the 1340 nm fluorescence band of Nd:NPs has not been previously used for *in vivo* imaging is its lower intensity when compared to the 900 and 1060 nm emission bands. Indeed, for most of the Nd^{3+} ion doped crystals the fluorescence branching ratio of the $^4F_{3/2}\rightarrow{}^4I_{13/2}$ (1340 nm) transition is about three times lower than that of the $^4F_{3/2}\rightarrow{}^4I_{9/2}$ (900 nm) or of $^4F_{3/2}\rightarrow{}^4I_{11/2}$ (1060 nm) transitions.[61, 63-65] As a matter of fact, generally speaking, only 15% of the radiative de-excitations generated from the $^4F_{3/2}$ metastable state of neodymium ions is produced through the $^4F_{3/2}\rightarrow{}^4I_{13/2}$ fluorescence channel.[66, 67] This implies that the use of the 900 or 1060 nm bands would provide brighter images than those obtained by exploiting the 1340 nm emission. Thus, the achievement of *in vivo* fluorescence imaging based on the 1340 nm weak emission would require the use of a host matrix providing large radiative de-excitation probabilities for Nd^{3+} ions. In this sense, the SrF_2 host seems to be particularly interesting as it has been shown to provide the highest emission intensities for other trivalent RE ions as compared to other fluoride nanocrystals. [68, 69] This superior performance is based on different causes. First of all, multiphonon relaxation

is made inefficient in this host due to the low wavenumbers of the vibrational modes.[70] Moreover, although the local site symmetry at the cationic sites is highly symmetric in the SrF_2 lattice (Oh), due to the necessity of charge compensation (Nd^{3+} replaces Ca^{2+} or it is Sr^{2+}??), non-centrosymmetric crystal field components around the neodymium ions are expected to be present, thereby leading to partially allowed forced electric dipole transition and, hence, to bright fluorescence. [71] Thus, in principle, Nd:SrF_2 NPs are expected to provide a highly intense 1340 nm emission, compared to other previously studied Nd:NPs. Consequently, we chose Nd:SrF_2 NPs for the first demonstration of *in vivo* fluorescence imaging at 1340 nm. **Figure 3 (a)** shows a Transmission Electronic Microscopy (TEM) image of the Nd:SrF_2 NPs used in this work as well as their size histogram. As can be observed, the synthetized Nd:SrF_2 NPs show a quasi-spherical morphology with an average diameter close to 10 nm and a size dispersion (FWHM) about of 4 nm. The as-synthesized Nd:SrF_2 NPs were easily dispersed in both water and phosphate saline buffer solution (PBS), showing an outstanding colloidal stability without any evidence of precipitation or agglomeration during a period of several months. **Figure 3 (b)** shows a digital picture of an aqueous solution of Nd:SrF_2 NPs (2.5 % wt in distilled water) together with the corresponding $^4F_{3/2} \rightarrow {}^4I_{13/2}$ (1340 nm) emission spectrum, obtained after exciting the solution with a 808 nm laser diode. Neodymium concentration in the SrF_2 host nanocrystals was 3 at.%. For the sake of comparison, we have also included the emission spectrum obtained under identical experimental conditions from an aqueous solution of Nd:LaF_3 (i.e. 2.5 % wt in distilled water) NPs. The Neodymium concentration in these NPs (having an average size of 15 nm) was 5 at. %. Nd:LaF_3 have been already successfully used for infrared *in vivo* imaging at circa 1060 nm.[54] In order to provide a proper comparison for both type of NPs (Nd:SrF_2 and Nd:LaF_3), the obtained fluorescence spectra given in Figure 3 (b) were normalized to the total number of Nd^{3+} ions present in each solution. The superior

performance (in terms of fluorescence intensity) of the Nd:SrF_2 NPs over the Nd:LaF_3 NPs in the 1300-1500 nm range is evident. The infrared emission in SrF_2 NPs is stronger than in LaF_3 NPs, despite the fact that in this last host the Nd^{3+} ions, replacing La^{3+} on the basis of a similar ionic radius, are accommodated in sites having a low Cs symmetry.[72, 73] As stated earlier, this fact could be due to the local charge compensation required when trivalent neodymium ions are incorporated in a divalent fluoride, as it could cause a strong non-inversion crystal field environment around the ions, giving rise to intense forced electric dipole transitions.[73] In order to get additional information to understand the excellent fluorescence performance of Nd:SrF_2 we have estimated their fluorescence Quantum Yield (QY) based on the previously determined yield (0.55, as obtained by thermal lens spectroscopy) for the Nd:LaF_3 NPs[60]. For this purpose we carefully measured the extinction spectra of our aqueous solution of Nd:SrF_2 and Nd:LaF_3 NPs. . As an example the extinction spectrum of the Nd:SrF_2/water solution is shown in **Figure 4**. The solution showed an almost negligible extinction coefficient in a wide spectral range (300-1300 nm) that can be explained in terms of the large band gap of the SrF_2 host together with a low scattering coefficient of the Nd:SrF_2 NPs. Inset in **Figure 4** shows the absorption coefficient (obtained by subtracting the scattering background to the extinction coefficient) in the 650-900 nm spectral range in which the optical transitions corresponding to Nd^{3+} ions are observed and properly labeled according to the involved transitions of this ion. Once the absorption coefficients are determined for the Nd^{3+} ions (at the excitation wavelength, 808 nm) in both NPs r the QY of the Nd:SrF_2 can be directly obtained NPs from the comparative emission spectra given in Figure 3 (b).In such a way we were able to estimate a fluorescence Q Y of of 0.9 ±0.1 for our Nd:SrF_2 NPs . Indeed, this large QY value can be now compared to that recently reported for Ag_2S Quantum Dots (QY = 0.15), that have been also used for high brightness infrared fluorescence in vivo imaging.[47]

2.3.- *In vivo* imaging and bio-distribution studies

Once the superior fluorescent properties (in terms of 1340 emitted intensity) of the Nd:SrF_2 NPs have been demonstrated, their potential application for high-contrast *in vivo* imaging was studied. For such purpose, we performed different infrared fluorescence imaging experiments by using a 808 nm diode laser as the excitation source and a Peltier cooled InGaAs infrared camera for detection. Two different experimental configurations were adopted. In the "*free-running*" mode (FRM) no filters were used such that the obtained fluorescence images accounted for the spatial distribution of emitted light integrated in the 900-1500 nm range. Additionally, fluorescence images were also obtained in the "*food fluorescence free*" mode (FFFM), by attaching a 1300 nm long pass filter to the camera objective. Thus, in this mode images were constructed by only recording the 1300-1500 nm fluorescence range. The complete removal of food fluorescence by using the FFFM configuration is demonstrated in **Figure 5**. **Figure 5(a)** shows an optical image of a food pellet and an Eppendorf partially filled with the aqueous solution of Nd:SrF_2 NPs. As can be observed in **Figure 5(b)**, both the food pellet and Nd:SrF_2 NPs appear in the FRM fluorescence image. This agrees well with the emission spectra included in **Figure 2,** where it is evident that a spectral overlap between food fluorescence and the $^4F_{3/2} \rightarrow {}^4I_{9/2}$ or $^4F_{3/2} \rightarrow {}^4I_{11/2}$ emission bands of Nd^{3+} ions occurs. At variance **Figure 5(c)** shows how the contribution of food emission to the fluorescence image is completely removed when images were acquired in the FFFM mode. The suitability of the 1340 nm emission of Nd:SrF_2 NPs for autofluorescence-free *in vivo* and *ex vivo* imaging is demonstrated in **Figures 5 (e)-(i)**. **Figures 5(e)** and **(f)** show the fluorescence images of a nude mouse (**Figure 5(d)**) after intravenous injection of 50 μL of a PBS solution containing Nd:SrF_2 NPs (at a concentration of 0.3% in mass), as obtained in the FRM and FFFM configurations, respectively. Both images were obtained 1 hour after injection using an excitation intensity 0.5 W/cm^2 at 808

nm. The FRM fluorescence image (**Figure 5(e)**) reveals a bright luminescence generated from the whole abdominal and lumbar zones. On the other hand, the FFFM (**Figure 5(f))** image provides a better resolution and larger contrast, denoting fluorescence only from a more localized zone at the upper area of the abdomen. Due to the complete absence of autofluorescence background, **Figure 5(f)** suggests a strong accumulation of Nd:SrF_2 NPs in the liver and/or spleen. This point has been further corroborated by performing *ex vivo* experiments. **Figures 5(h)** and **5(i)** show the fluorescence *ex vivo* images of the same mouse but after being sacrificed as obtained in both FRM and FFFM configurations, respectively. **Figure 5(i)** confirms that infrared fluorescence was mainly generated from the liver and spleen, without relevant contribution from other organs such as lungs or kidneys.

Complete removal of autofluorescence is not only required to get high contrast fluorescence *in vivo* images but also to extract reliable information about the biodistribution of intravenously injected NPs. As a general procedure, long-term biodistribution of NPs in small animals is studied by measuring the NPs fluorescence intensity generated by the different organs after removal from dissected animals at different times after the injection of the NPs. The amount of NPs retained in each organ is, then, estimated from the measured fluorescence intensity. Obviously, this procedure is only valid when there is absolute certainty that no background fluorescence is present. Otherwise, it is not possible to establish a linear relation between fluorescence intensity and amount of retained NPs. **Figure 6(a)** shows the fluorescence images, as obtained in both FRM and FFFM configurations, of the different organs removed from a mouse sacrificed 1 hour after the intravenous injection of Nd:SrF_2 NPs. In the fluorescence images obtained in FRM configuration several organs, in addition to liver and spleen, produce significant fluorescence. Indeed, this could lead to the wrong bio distribution pattern shown in **Figure 6(b)**. Indeed, fluorescence images obtained in the 1300-1500 nm spectral range (i.e. FFFM configuration) reveal that the Nd:SrF_2 NPs have only been

retained by the liver and spleen. Thus, the reliable biodistribution diagram is simpler than that shown in **Figure 6(c)**. These results can be now compared to those previously reported in the literature concerning short and long term biodistribution of nanoparticles in mice. Yang et al. have studied the biodistribution of PEG coated nano-graphene sheets (NGSs) in mice, concluding that 1 hour after injection they were accumulated in diverse organs including lungs, heart, kidney, liver and spleen. [74] They also found that for longer times (24 h after injection) the number of NGSs accumulated in lungs, heart and liver decreased whereas those accumulated in spleen and kidneys increased. [74] Similarly, Faraj et al. found that 1 day after injection of carbon nanotubes (CNTs) they were preferentially accumulated in the liver.[75] Lao et al. studied in detail the biodistribution of carboxylated-polystyrene NPs, with diameters ranging from 20 nm up to 500 nm, 4 hours after intravenous injection in mice. [76] For the smallest NPs (20 nm in diameter) Lao et al found that the NPs were accumulated/retained mainly in the liver. Naczynski et al. investigated the time-resolved biodistribution of rare earth doped infrared NPs in mice after intravenous injection.[59] They found that RENPs were efficiently retained by the liver for post injection times larger than 1 minute.[59] This result is also in agreement with previous works dealing with the dynamical biodistribution of CNTs intravenously injected in mice.[77] Thus, the biodistribution pattern of Nd:SrF_2 NPs included in **Figure 6(c),** that points out preferential NP accumulation by liver and spleen, is found to be in reasonable agreement with those previously found for other LNPs.

It is widely assumed that bio-distribution of intravenously injected NPs is also strongly determined by the particular surface charge of the injected NPs. This charge dependence is correlated with the binding to different proteins as a result of the different NP charges. Indeed, as an example, S. Hirn et al. found that negatively charged Gold NPs intravenously injected in mice preferentially accumulated at liver whereas positively charged ones displayed a larger accumulation rate in the other organs.[78] A similar conclusion was reached

by Xiao et al. who demonstrated a preferential uptake rate of negatively charged NPs by both the liver and spleen. [69, 79] These results agree with the study carried out by Balogh et al. who systematically studied the relevance of NPs surface charge in the biodistribution patterns of intravenously injected Gold nanocomposite devices; again it was found that, when injected NPs were negatively charged, they were mainly accumulated at liver and spleen.[80] As described in the experimental section, our Nd:SrF_2 NPs are negatively charged with a Z potential close to -25 mV. Thus, according to the mentioned works, it is expected that they accumulate preferentially in both liver and spleen, as it has been experimentally observed.

According to most of the above-mentioned works it is clear that the biodistribution pattern of LNPs in mice is also strongly time dependent. In order to check for the possible time dependence of Nd:SrF_2 NPs accumulation by different organs we intravenously injected the same dose of Nd:SrF_2 NPs (50 μL of an 0.3 % in mass concentrated aqueous solution) in 5 different mice. Then these mice were sacrificed at different times after injection (1h, 4, 24, 48 and 72 hours) and the *ex vivo* fluorescence images were systematically acquired (see **Figure 7(a)**) in the FFFM configuration. From these images we have found that the amount of Nd:SrF_2 NPs accumulated in liver and spleen follow a completely different time evolution. This is clearly observed in **Figure 7(b)**, which shows the fluorescence signal generated from the liver and spleen as well as the total fluorescence intensity (resulting from the sum of the fluorescence intensities generated by the liver and spleen). As can be observed, at short times (< 20 hours after injection) Nd:SrF_2 NPs were mainly retained by the liver whereas for longer times, the fluorescence generated from the spleen becomes dominant. This fact reveals a dynamical transfer of Nd:SrF_2 NPs from the liver to the spleen during the first 80 hours after intravenous injection. The different time evolution of the fluorescence generated from both liver and spleen is more evident in **Figure 7(c)**, which shows the time evolution of the fluorescence intensities from these two organs normalized to their respective weight. At this

point it should be mentioned that the observed preferential uptake of Nd:SrF_2 NPs by the highly perfused organs, such as liver and spleen, is very likely due to the presence of macrophages in their tissues, which are responsible for capturing particulates and macromolecules circulating in the blood.[81] The results included in **Figures 6 and 7** points to the fact that Nd:SrF_2 NPs could behave as promising high penetration infrared contrast agents for dynamical fluorescence anatomical *in vivo* imaging. This, however, would require appropriate surface functionalization for tailoring of both surface charge and affinity while ensuring long circulation times.[82]

2.4.- *Toxicity studies*

Finally, with regards to the possible toxicological effects of the Nd:SrF_2 NPs, we systematically investigated the possible presence of either behavioral changes or weight loss in mice after intravenous injection. **Figure 8** shows the body weight variations of a group of animals (n = 3 mice) after intravenous injection of an identical dose of Nd:SrF_2 NPs as that used throughout the previously described *in vivo* fluorescence imaging experiments (50 μL of an 0.3% in mass concentrated PBS solution of Nd:SrF_2 NPs). For the sake of comparison the body weight variation of a "control" group (n = 3 mice) intravenously injected with the same volume (50 μL) of PBS, has also been included. During the time period studied, 24 days, no significant differences between the average weight evolution of the Nd:SrF_2 injected mice and the control group were observed. During this period of time both injected and control mice were systematically observed trying to determine any significant difference between their behavior or external appearance; again, no significant differences were observed. Thus, from these observations we concluded that the Nd:SrF_2 NPs do not cause appreciable toxicity ate least up to the injection doses required for high contrast in vivo fluorescence imaging.

This result is in agreement with those reported for other imaging NPs, such as metallic ones. [83]

The *in vitro* cytotoxicity of the Nd:SrF_2 NPs has been also investigated by the MTT assay approach, as described in detail in the Methods Section. The toxicity of the SrF_2 nanoparticles was investigated in HeLa cells after incubation with a medium containing SrF_2 NPs at different concentrations (25, 50 and 100 μg/mL). As can be observed in **Figure 9**, noevidence of relevant cytotoxicity has been found for the concentrations and incubation times studied in this work. At this point we would like to note that the incubation times and concentrations used in the cytotoxicity experiments were those required for in vitro fluorescence imaging of HeLa cancer cells based on SrF_2 NPs. This is evidenced in the inset of **Figure 9,** that shows the fluorescence image of HeLa cancer cells incubated during 2 hours in a PBS solution containing Nd:SrF_2 NPs at a concentration of 50 μg/mL. Infrared *in vitro* fluorescence image evidences the adhesion of Nd:SrF_2 NPs to the cell membrane.

3.- CONCLUSIONS

In summary, we have demonstrated how the use of the particular emission band at 1340 nm of Nd^{3+} ions in SrF_2 NPs can be used for deep tissue, autofluorescence free, high resolution *in vivo* imaging. This is based on the null spectral overlap between this emission band and the infrared autofluorescence generated by the animal's food. The complete removal of infrared autofluorescence has allowed us to record high contrast *in vivo* fluorescence images as well as to carry out reliable biodistribution studies of Nd:SrF_2 nanoparticles in mice. We have found that these RENPs are initially accumulated in the liver although a dynamical transfer from liver to spleen takes place on a day timescale. Finally, the possible presence of toxicological effects associated to intravenous injection of Nd:SrF_2 NPs

have been investigated concluding that, at the doses required for high contrast *in vivo* imaging, the Nd:SrF_2 NPs result in a negligible toxicity. The high brightness, high chemical and physical stability as well as high biocompatibility makes Nd:SrF_2 NPs very promising infrared nanoprobes for *in vivo* imaging experiments in the second biological window.

4.- METHODS

Synthesis of SrF_2 nanoparticles. The preparation of the lanthanide doped SrF_2 NPs has been previously described by Pedroni et al..[69] Briefly, stoichiometric amounts of the lanthanide chlorides and strontium chlorides were dissolved in 7 ml of de-ionized water (total metal amount of 3.5 mmol). To this solution, 20 ml of a 1 M solution of potassium citrate were added dropwise under vigorous stirring for a few minutes. Then, an amount of 8.75 mmol of ammonium fluoride was added to the previous solution. The resultant clear solution was heated in a 50 ml stainless steel Teflon lined digestion pressure vessel at 190 °C for 6 h. After washing with acetone and drying at room temperature, the obtained NPs were directly dispersed in water.

Surface charge, structure and morphology of the nanoparticles. Zeta-potential of the NPs was measured using a Malvern Zetasizer Nano ZS90 operating with a He-Ne laser at 633 nm. Measurements were carried out in water colloidal dispersions of SrF_2 NPs with a 25 g/L concentration. A Zeta-potential value of -24±9 mV was found. It is worth to remark that a negative value of the Zeta-potential has been also found for Tm^{3+},Yb^{3+} doped alkaline-earth fluoride NPs.[69]

X-ray analysis. The X-Ray powder diffraction (XRPD) pattern was measured with a powder diffractometer (Thermo, ARL XTRA), operating in Bragg-Brentano geometry, equipped with a Cu-anode X-ray source (K_α=1.5418) and using a Peltier Si(Li) cooled solid state detector. The pattern was collected at a scan rate of 0.04 °/min the 15°-90° 2θ range. The powdered sample was finely ground in a mortar and then deposited in a low-background sample stage for the measurements. A structural analysis revealed that the present SrF_2 nanoparticles are single phase with a cubic fluorite structure. The calculated lattice parameter for the cubic cell is of 5.774(1) Å, slightly higher than that found for Tm^{3+},Yb^{3+} doped SrF_2 nanoparticles.[69]

TEM measurements. The size and morphology of the Neodymium doped SrF_2 nanoparticles were determined by using a Transmission Electron Microscope (TEM, JEOL JEM1010)

working at 80 kV of accelerating voltage. The histograms to obtain the size dispersion were made from the analysis of several images by using the Mac Biophotonics-Image J software.

Fluorescence measurements. Fluorescence measurements were carried out in a conventional confocal fluorescence microscope. A fiber coupled laser diode (Lumics LU0808M100) operating at 808 nm (peak of the $^4I_{9/2} \rightarrow {}^4F_{5/2}$ absorption band) was used as excitation beam. Pump beam was focused into the Nd:SrF_2 solution by using a 50× infrared microscope objective (0.55 NA). The subsequent fluorescence was collected by the same objective and spectrally analyzed by a nitrogen cooled AsGAIn array connected to a high resolution monochromator (IR550M). The spectral response of the whole detection system (including microscope objective, monochromator and detector) was experimentally obtained by measuring the emission spectra of reference samples such as Nd:YAG crystals and incandescent lamps.

Food autofluorescence spectrum acquisition.-Figure 2 (a) includes the fluorescence images of a food pellet under 808 nm excitation, as obtained by using a set of different long-pass filters with cut-off wavelengths ranging from 900 up to 1400 nm. The wavelength dependence of the food fluorescence was obtained from the analysis of these images. The total (integrated) fluorescence intensity generated by the food pellet was calculated from each fluorescence image. This integrated intensity is denoted as I_λ^{int} where λ is the cut-off wavelength of the longpass filter used for image acquisition. We have used longpass filters with cut-off wavelengths increasing in 50 nm steps. Subtracting the integrated fluorescence intensities obtained by two consecutive longpass filters ($I_\lambda^{int} - I_{\lambda+50\,nm}^{int}$) the difference gives the intensity generated by the food pellet in the spectral range ranging from λ up to $\lambda + 50\,nm$. This could be, in a first order approximation, identified as the fluorescence intensity emitted by the food pellet at a wavelength of $\lambda + 25\,nm$ that is the medium wavelength between $\lambda$and $\lambda + 50\,nm$. Thus, if we denote the fluorescence intensity emitted by the food pellet at a wavelength of $\lambda + 25\,nm$ by $I_{\lambda+2\,5nm}$then this term has been to be proportional to $I_\lambda^{int} - I_{\lambda+50\,nm}^{int}$ in such a way that $I_{\lambda+2\,5nm} \propto I_\lambda^{int} - I_{\lambda+50\,nm}^{int}$.

Toxicity studies.- The MTT (3-(4,5-dimethylthiazol-2-yl)-2,5-diphenyltetrazolium bromide) assay is a simple non-radioactive colorimetric assay to measure cell cytotoxicity, proliferation or viability. MTT is a yellow, watersoluble, tetrazolium salt. Metabolically active cells are able to convert this dye into a water-insoluble dark blue formazan by reductive cleavage of the tetrazolium ring [T. Mosmann, Rapid colorimetric assay for cellular growth and survival: application to proliferation and cytotoxic assay. Formazan crystals, then, can be dissolved in an organic solvent such as dimethylsulphoxide

(DMSO) and quantified by measuring the absorbance of the solution at 540 nm, and the resultant value is related to the number of living cells. To determine cell cytotoxicity/viability, the cells were plated in a 24 well plate at 37 ºC in 5% CO_2 atmosphere. After 48 h of culture, the medium in the well was replaced with the fresh medium containing Nd:SrF_2 nanoparticles of three different concentrations (25, 50 and 100 µg/ml) and HeLa cells were incubated for different periods of time ranging from 2 up to 48 hours. After incubation, the medium was removed and added completed medium without nanoparticles. After 24 h, 0.5 ml of MTT dye solution (0.05 mg/ml of MTT, Sigma) was added to each well. After 2-3 h of incubation at 37 ºC and 5% CO_2, the medium was removed and formazan crystals were solubilized in 0.5 ml of DMSO (Merck) and the solution was vigorously mixed to dissolve the reacted dye. The absorbance at 540 nm was read using a microplate reader (Espectra Fluor 4, Tecan). The % of viability of HeLa cells incubated with NPs as compared to control cells (i.e. without incubation with nanoparticles) was calculated as [A] test/[A] control x 100, where [A] test is the absorbance of the tested sample and [A] control is the absorbance of the control sample.

In vitro **imaging.-** Fluorecence image sof HeLa cells incubated with Nd:SrF_2 NPs have been optained with an epi-fluorescence microscope equipped with an AsGaIn camera with enhanced sensitivity in the 850-1500 nm spectral range. Excitation was performed by using a 808 nm fiber coupled diode. Excitation radiation was blocked by using a longpass filter with a cut-off wavelength of 850 nm.

In vivo **experiments**. In vivo experiments. Fluorescence in vivo imaging was performed by using a peltier colled AsGaIn camera (XEVA 1.7, Xenics Corp) coupled to a C-Mount objective. A long-pass filter blocking all wavelengths below 850 nm (FEL1000 from Thorlabs GmbH) was continuously attached to the C-Mount objective in order to remove any contribution from the 808 nm laser scattered radiation. The C-Mount objective was attached to a filter wheel equipped with six long pass filters with cut-off wavelengths ranging from 900 up to 1400 nm. Laser excitation was achieved by using a fiber coupled laser diode (LIMO GmmH). The excitation intensity of 808 nm irradiation was always kept below 1 W/cm2. For all the in vivo experiments, 50 µl of a solution of Nd:SrF_2 NPs dispersed in Phosphate Buffered Saline (PBS, at a concentration of 0.3 % in mass) were intravenously injected through the retro-orbital sinus into 9-week-old female CD1 mice. For the in vivo imaging, the previously shaved mice were anesthetized with 2% isoflurane. For monitoring the weight evolution, the animals were weighted daily at the same time during 30 days after the inoculation. The average weight and the standard deviation were calculated and represented for each time point in order to establish the comparisons between NPs-inoculated

mice and their corresponding controls inoculated with PBS, including n = 3 animals per group. Mice were housed and maintained under specific pathogen-free conditions and all the experimental procedures with animals were carried out in compliance with the guidelines in RD 53/2013 (Spain) and were approved by the Ethics Committee from Universidad Autonoma of Madrid (CEIT) in the frame of the project FIS-PI12/01253 supported by the Spanish Ministerio de Economía y Competitividad.

Acknowledgements

This work was supported by Fondazione Cariverona (Verona, Italy), project "Verona Nanomedicine Initiative". Work also supported by the Ministerio de Innovación y Ciencia of Spain under project MAT2010-16161. Patricia Haro thanks the Spanish Ministerio de Economia y Competitividad (MINECO) for a Juan de la Cierva grant. The authors also thank the Brazilian agencies FAPEAL-Fundação de Amparo a Pesquisa do Estado de Alagoas (Project PRONEX 2009-09-006), FINEP (Financiadora de Estudos e Projetos), CNPq (Conselho Nacional de Desenvolvimento Científico e Tecnológico) through Grant INCT NANO(BIO)SIMES, and CAPES (Coordenadoria de Aperfeiçoamento de Pessoal de Ensino Superior). D. Jaque (Pesquisador Visitante Especial(PVE)-CAPES) thanks the CAPES by means of the Project PVE number A077/2013.

FIGURES

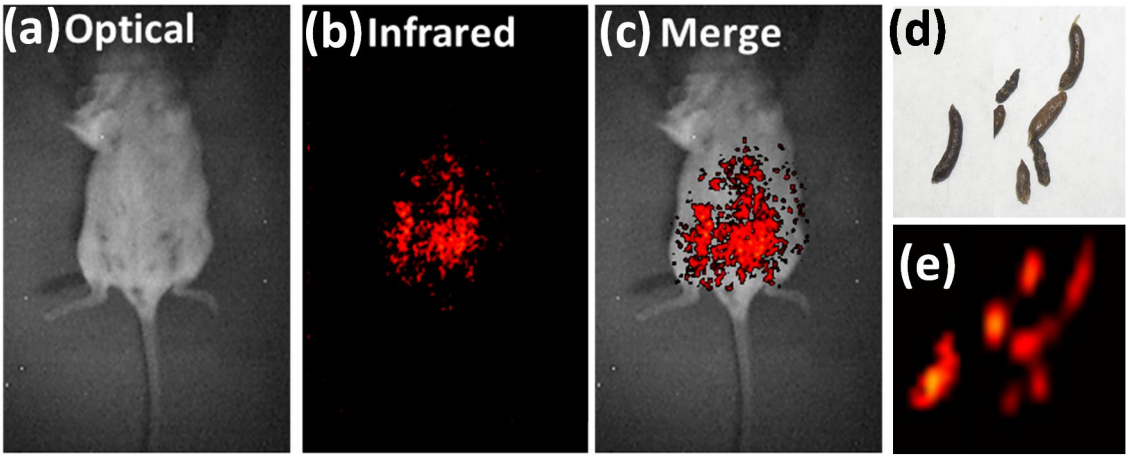

Figure 1.- (a) Optical, **(b)** fluorescence and **(c)** merged images of a control mouse. **(d)** optical image of several dregs as obtained from a conventionally fed mouse. **(e)** Infrared fluorescence image of the dregs. Fluorescence images were obtained with an InGaAs camera with a 900 nm long pass filter, so they account for the total emitted intensity between 900 and 1500 nm.

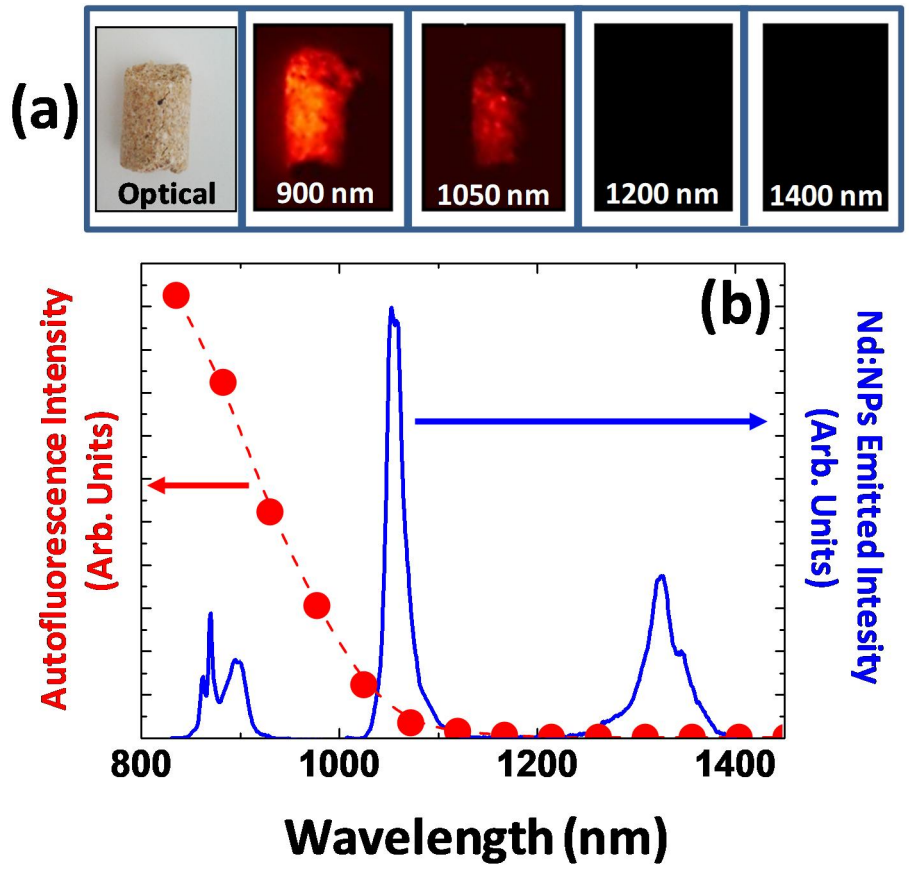

Figure 2.- (a).- Optical image of a mouse food pellet and fluorescence images of the same pellet as obtained using different longpass filters when excited with a 808 nm laser. **(b).-** Wavelength dependence of the infrared autofluorescence intensity generated by a mouse food pellet. Dots are experimental data and dashed line is a guide for the eyes. This figure also includes the room temperature emission spectrum (un-corrected by the detection system spectral response) of a colloidal solution of Nd:SrF_2 nanoparticles.

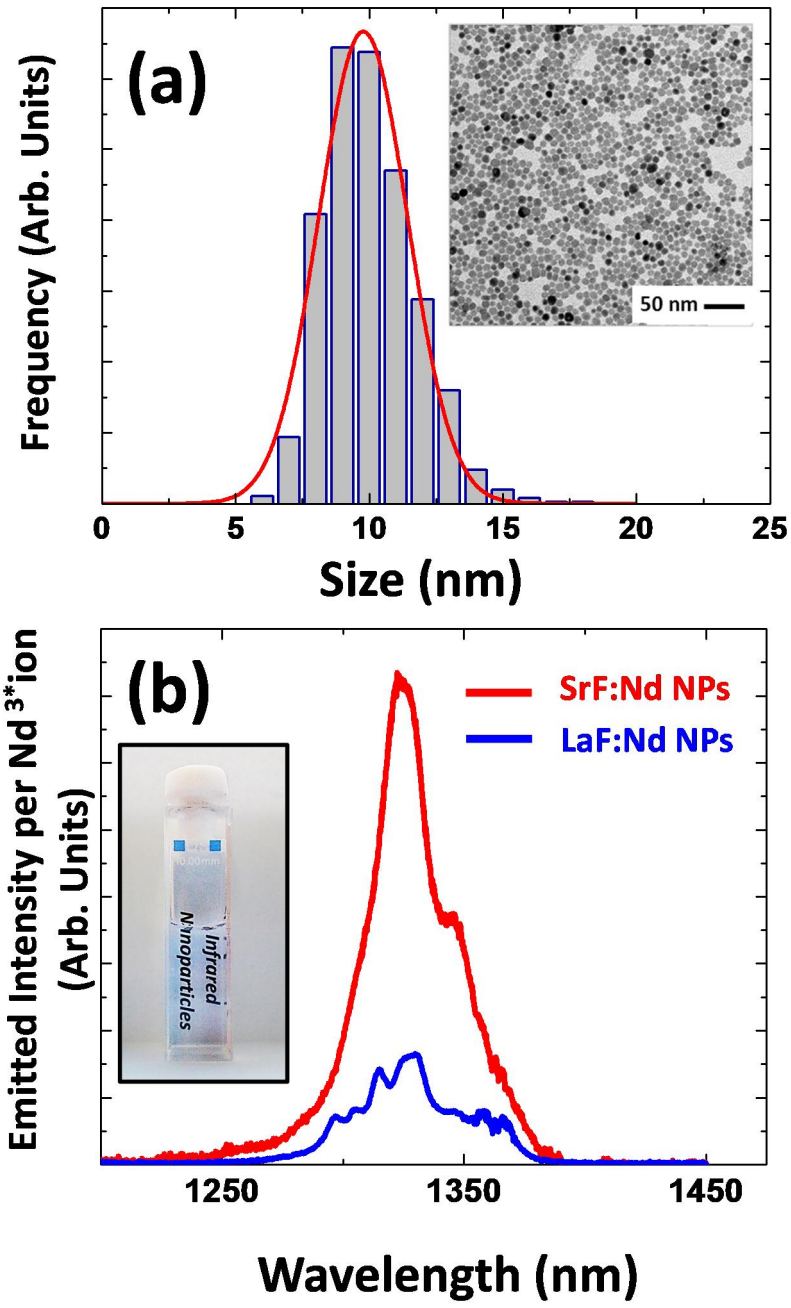

Figure 3.- (a)- Size distribution of the Nd:SrF_2 NPs used in this work as obtained from the statistical analysis of the TEM image included as an inset. **(b).-** Infrared emission spectrum as obtained from an aqueous colloidal solution of Nd:SrF_2 NPs (see inset). For the sake of comparison we also include the emission spectrum obtained in exactly the same experimental conditions for a colloidal suspension of Nd:LaF_3 NPs. In both cases the fluorescence intensity has been corrected by the number of Nd^{3+} ions in each system.

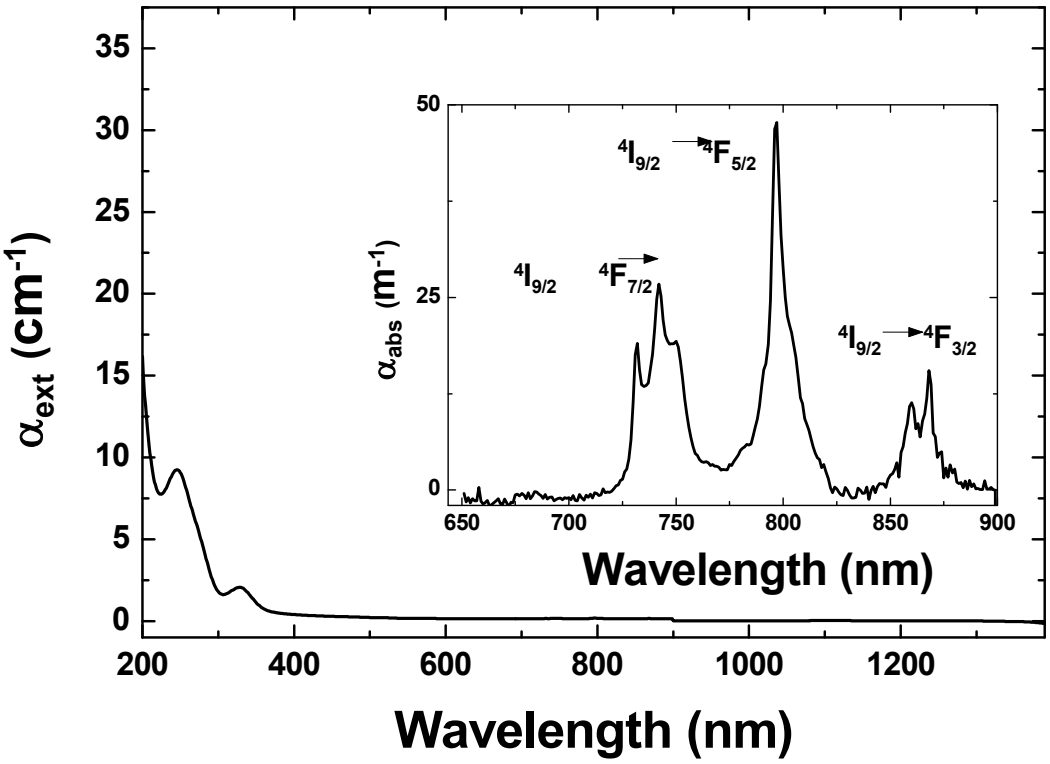

Figure 4.- Room temperature extinction coefficient in the 200-1400 nm spectral range as obtained for a colloidal solution of Nd:SrF_2 nanoparticles. The nanoparticle concentration was set to 25 mg/mL. Inset shows the absorption coefficient as obtained by subtracting the scattering background to the extinction coefficient.

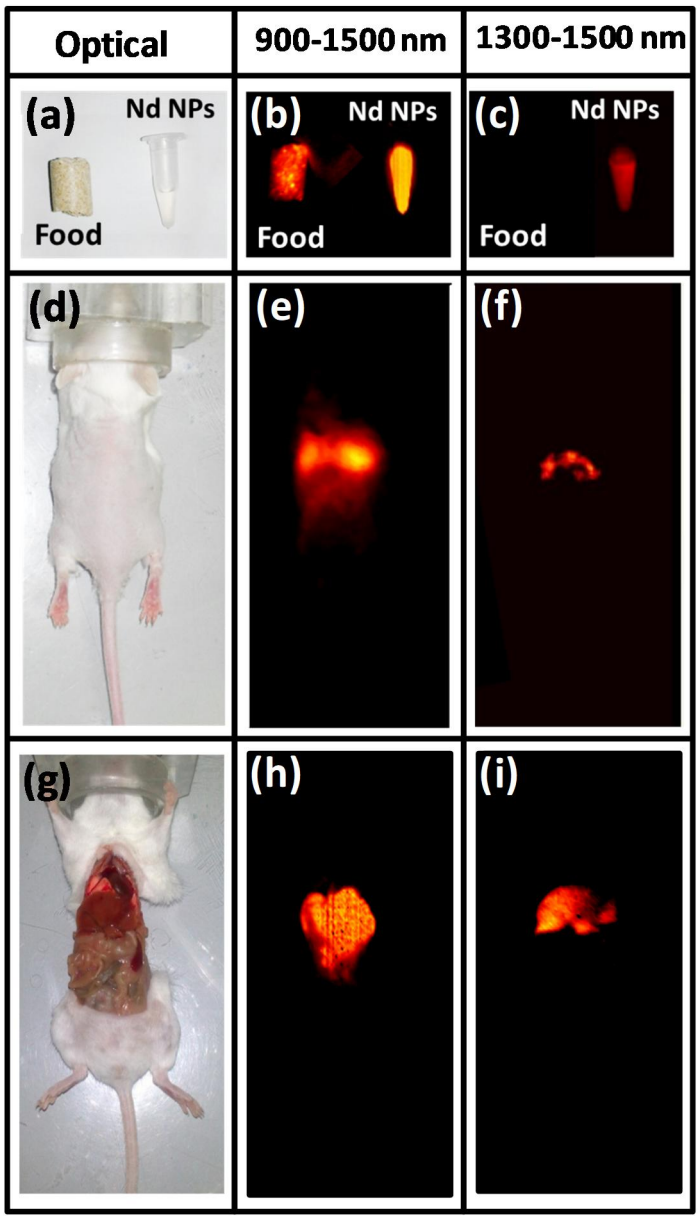

Figure 5.- Left Column.- Optical image of a mouse food pellet, an eppendorf containing a colloidal solution of Nd:SrF_2 NPs **(a)**, of a living mouse after intravenous administration through the retro-orbital venous sinus of 50 μL of a colloidal solution of Nd:SrF_2 NPs in phosphate buffered saline (**(d)**) and of the same mouse after being sacrificed and opened to get direct access to organs (**(g)**). **Middle column.-** Corresponding fluorescence images of the three systems under 808 nm illumination as obtained by recording fluorescence in the 900-1500 nm range**. Right column.-** Fluorescence images also obtained under 808 nm excitation but in this case recording fluorescence intensity in the 1300-1500 nm range.

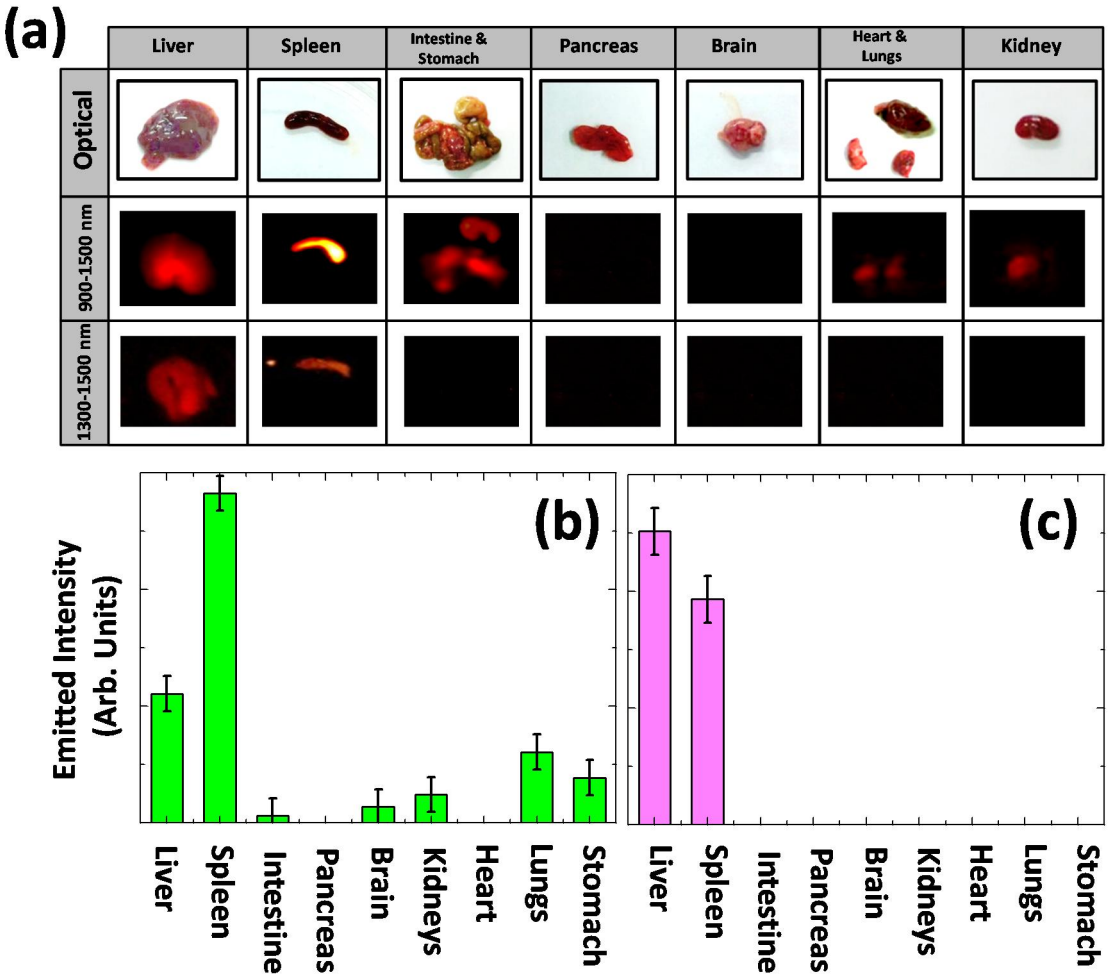

Figure 6.- **(a)** - Optical images and fluorescence images in the 900-1500 and 1300-1500 nm spectral detection ranges of the organs extracted from a sacrificed mouse 1 hours after an intravenous injection of Nd:SrF_2 NPs. **(b)** 900-1500 nm integrated fluorescence intensity obtained from the different organs. **(c)** 1300-1500 nm integrated intensity obtained from the different organs. In all cases, the integrated fluorescence intensity has been normalized by the organ´s weight.

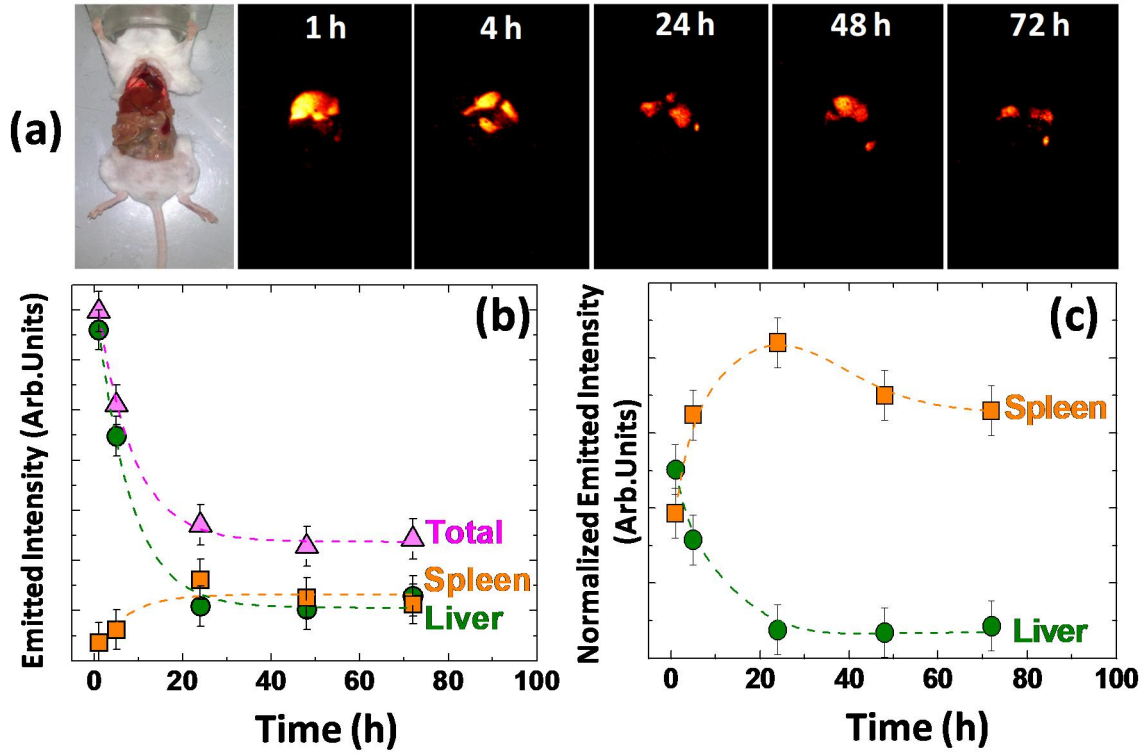

Figure 7.- **(a)-** *Ex vivo* fluorescence images (obtained in the 900-1500 nm detection spectral range) corresponding to different mice sacrificed at different times from the intravenous injection of Nd:SrF_2 NPs. **(b).-** Integrated fluorescence intensity obtained from the liver and spleen as a function of the time elapsed between injection and *ex vivo* image procedure. **(c).-** Evolution of the weight normalized fluorescence from the liver and spleen as a function of the time elapsed between injection and *ex vivo* image procedure. Dots are experimental data and dashed lines are guides for the eyes.

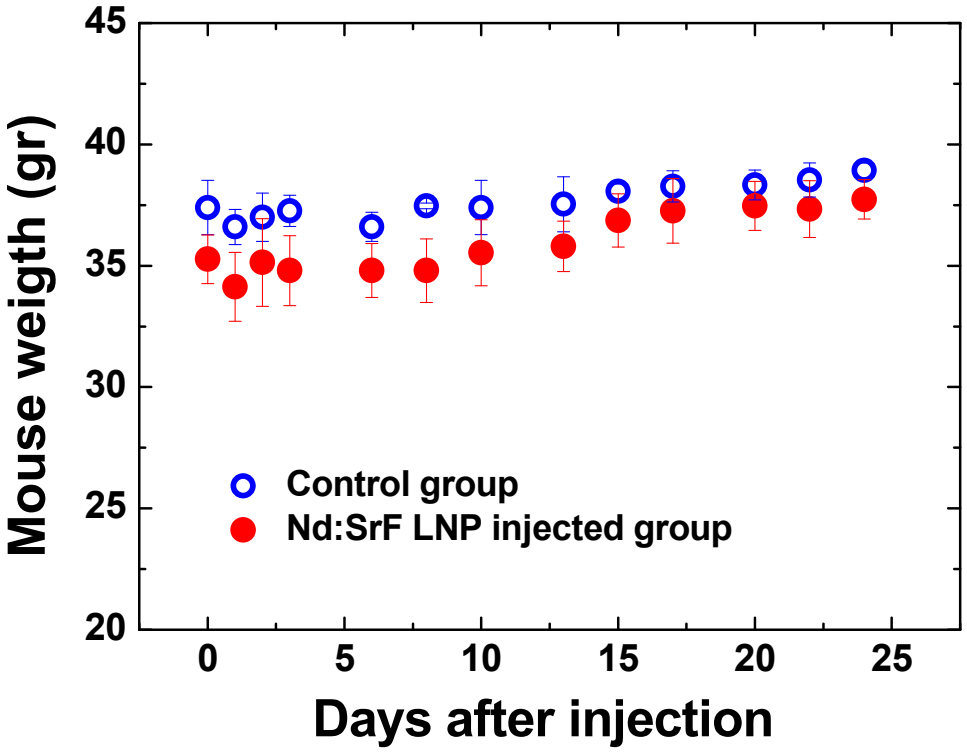

Figure 8.- Time evolution of the averaged weight (calculated over 3 individuals) after intravenous injection of Nd:SrF_2 NPs. The time evolution of the averaged weight calculated over 3 control mice has been also included. Error bars correspond to the weight standard deviation in each group.

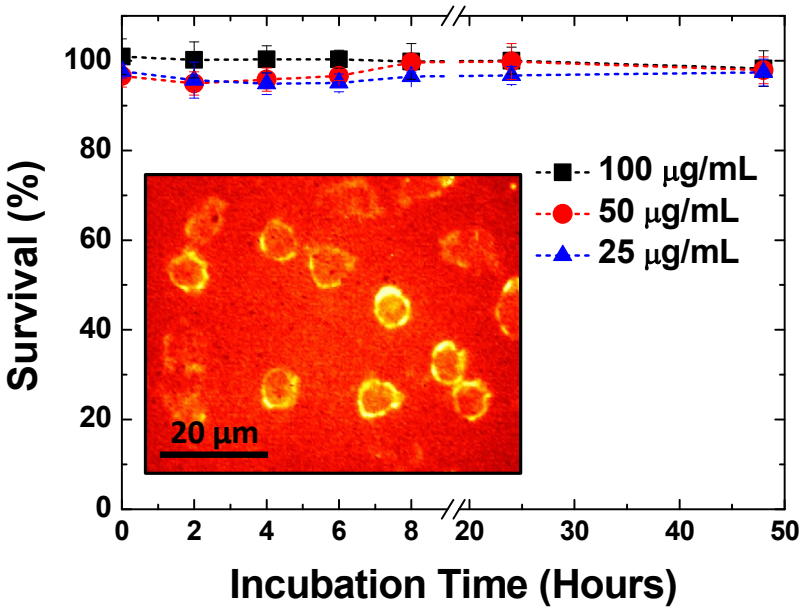

Figure 9.- Percent survival of HeLa cell line incubated with different concentrations of Nd:SrF_2 NPs for different incubation times. Each experimental point (dot) corresponds to the mean value (SD) obtained from three different experiments. Inset shows the fluorescence infrared (850-1450 nm) image of HeLa cells incubated with a Nd:SrF_2 solution (50 μg/mL) during 2 hours.

REFERENCES

1. Srinivas, P. R.; Barker, P.; Srivastava, S. *Laboratory investigation; a journal of technical methods and pathology* **2002,** 82, (5), 657-62.
2. Szelenyi, I. *Inflammation Research* **2012,** 61, (1), 1-9.
3. Ferrari, M. *Nat. Nanotechnol.* **2007,** 2, (8), 37-47.
4. Nie, S. M.; Xing, Y.; Kim, G. J.; Simons, J. W., Nanotechnology applications in cancer. In *Annual Review of Biomedical Engineering*, 2007; Vol. 9, pp 257-288.
5. Liu, Y.; Miyoshi, H.; Nakamura, M. *International Journal of Cancer* **2007,** 120, (12), 2527-2537.
6. Davis, S. S. *Trends Biotechnol.* **1997,** 15, (6), 217-224.
7. Alivisatos, A. P. *Scientific American* **2001,** 285, (3), 66-73.
8. Bao, G.; Mitragotri, S.; Tong, S. *Annual Review of Biomedical Engineering, Vol 15* **2013,** 15, 253-282.
9. Willner, I.; Willner, B. *Nano Letters* **2010,** 10, (10), 3805-3815.
10. Brigger, I.; Dubernet, C.; Couvreur, P. *Advanced Drug Delivery Reviews* **2002,** 54, (5), 631-651.
11. Pankhurst, Q. A.; Thanh, N. T. K.; Jones, S. K.; Dobson, J. *Journal of Physics D-Applied Physics* **2009,** 42, (22).
12. Dreaden, E. C.; Alkilany, A. M.; Huang, X. H.; Murphy, C. J.; El-Sayed, M. A. *Chemical Society Reviews* **2012,** 41, (7), 2740-2779.
13. Rojas-Chapana, J. A.; Giersig, M. *Journal of Nanoscience and Nanotechnology* **2006,** 6, (2), 316-321.
14. Juzenas, P.; Chen, W.; Sun, Y. P.; Coelho, M. A. N.; Generalov, R.; Generalova, N.; Christensen, I. L. *Advanced Drug Delivery Reviews* **2008,** 60, (15), 1600-1614.
15. Idris, N. M.; Gnanasammandhan, M. K.; Zhang, J.; Ho, P. C.; Mahendran, R.; Zhang, Y. *Nature Medicine* **2012,** 18, (10), 1580-U190.
16. Huff, T. B.; Tong, L.; Zhao, Y.; Hansen, M. N.; Cheng, J. X.; Wei, A. *Nanomedicine* **2007,** 2, (1), 125-132.
17. Jaque, D.; Vetrone, F. *Nanoscale* **2012,** 4, (15), 4301-4326.
18. Gnach, A.; Bednarkiewicz, A. *Nano Today* **2012,** 7, (6), 532-563.
19. Crisp, M. T.; Kotov, N. A. *Nano Letters* **2003,** 3, (2), 173-177.
20. Sperling, R. A.; Parak, W. J. *Philosophical Transactions of the Royal Society A: Mathematical, Physical and Engineering Sciences* **2010,** 368, (1915), 1333-1383.
21. Cañaveras, F.; Madueño, R.; Sevilla, J. M.; Blázquez, M.; Pineda, T. *The Journal of Physical Chemistry C* **2012,** 116, (18), 10430-10437.
22. Saravanakumar, G.; Kim, K.; Park, J. H.; Rhee, K.; Kwon, I. C. *Journal of Biomedical Nanotechnology* **2009,** 5, (1), 20-35.
23. Naccache, R.; Rodriguez, E. M.; Bogdan, N.; Sanz-Rodriguez, F.; Cruz, M. D. C. I. d. l.; Fuente, A. J. d. l.; Vetrone, F.; Jaque, D.; Sole, J. G.; Capobianco, J. A. *Cancers* **2012,** 4, (4), 1067-105.
24. Ruedas-Rama, M. J.; Walters, J. D.; Orte, A.; Hall, E. A. H. *Analytica Chimica Acta* **2012,** 751, 1-23.
25. Jacques, S. L. *Physics in Medicine and Biology* **2013,** 58, (14), 5007-5008.
26. Bhaumik, S.; DePuy, J.; Klimash, J. *Lab Animal* **2007,** 36, (8), 40-43.
27. Taroni, P.; Pifferi, A.; Torricelli, A.; Comelli, D.; Cubeddu, R. *Photochem. Photobiol. Sci.* **2003,** 2, (2), 124-129.
28. Frangioni, J. V. *Current Opinion in Chemical Biology* **2003,** 7, (5), 626-634.
29. Smith, A. M.; Mancini, M. C.; Nie, S. M. *Nat. Nanotechnol.* **2009,** 4, (11), 710-711.
30. Venkatachalam, N.; Yamano, T.; Hemmer, E.; Hyodo, H.; Kishimoto, H.; Soga, K. *Journal of the American Ceramic Society* **2013,** 96, (9), 2759-2765.

31. Hemmer, E.; Venkatachalam, N.; Hyodo, H.; Hattori, A.; Ebina, Y.; Kishimoto, H.; Soga, K. *Nanoscale* **2013,** 5, (23), 11339-11361.
32. Nyk, M.; Kumar, R.; Ohulchanskyy, T. Y.; Bergey, E. J.; Prasad, P. N. *Nano Letters* **2008,** 8, (11), 3834-3838.
33. Zhou, J.; Liu, Z.; Li, F. Y. *Chemical Society Reviews* **2012,** 41, (3), 1323-1349.
34. Wang, F.; Liu, X. *J Am Chem Soc* **2008,** 130, (17), 5642-3.
35. Yang, Y.; Shao, Q.; Deng, R.; Wang, C.; Teng, X.; Cheng, K.; Cheng, Z.; Huang, L.; Liu, Z.; Liu, X. *Angewandte Chemie International Edition* **2012,** 51, (13), 3125-3129.
36. Maldiney, T.; Viana, B.; Bessiere, A.; Gourier, D.; Bessodes, M.; Scherman, D.; Richard, C. *Optical Materials* **2013,** 35, (10), 1852-1858.
37. Basavaraju, N.; Sharma, S.; Bessiere, A.; Viana, B.; Gourier, D.; Priolkar, K. R. *Journal of Physics D-Applied Physics* **2013,** 46, (37).
38. Lecointre, A.; Bessiere, A.; Priolkar, K. R.; Gourier, D.; Wallez, G.; Viana, B. *Materials Research Bulletin* **2013,** 48, (5), 1898-1905.
39. le Masne de Chermont, Q.; Chanéac, C.; Seguin, J.; Pellé, F.; Maîtrejean, S.; Jolivet, J.-P.; Gourier, D.; Bessodes, M.; Scherman, D. *Proceedings of the National Academy of Sciences* **2007,** 104, (22), 9266-9271.
40. Inoue, Y.; Izawa, K.; Kiryu, S.; Tojo, A.; Ohtomo, K. *Molecular Imaging* **2008,** 7, (1), 21-27.
41. Troy, T.; Jekic-McMullen, D.; Sambucetti, L.; Rice, B. *Molecular imaging* **2004,** 3, (1), 9-23.
42. Krasnovsky, A. A., Jr.; Kovalev, Y. V. *Biochemistry Moscow* **2014,** 79, (4), 349-361.
43. Welsher, K.; Sherlock, S. P.; Dai, H. *Proceedings of the National Academy of Sciences of the USA* **2011,** 108, (22), 8943-8948.
44. Hong, G. S.; Robinson, J. T.; Zhang, Y. J.; Diao, S.; Antaris, A. L.; Wang, Q. B.; Dai, H. J. *Angewandte Chemie-International Edition* **2012,** 51, (39), 9818-9821.
45. Li, C.; Zhang, Y.; Wang, M.; Zhang, Y.; Chen, G.; Li, L.; Wu, D.; Wang, Q. *Biomaterials* **2014,** 35, (1), 393-400.
46. Zhang, Y.; Zhang, Y.; Hong, G.; He, W.; Zhou, K.; Yang, K.; Li, F.; Chen, G.; Liu, Z.; Dai, H.; Wang, Q. *Biomaterials* **2013,** 34, (14), 3639-3646.
47. Zhang, Y.; Hong, G.; Zhang, Y.; Chen, G.; Li, F.; Dai, H.; Wang, Q. *ACS Nano* **2012,** 6, (5), 3695-3702.
48. Du, Y.; Xu, B.; Fu, T.; Cai, M.; Li, F.; Zhang, Y.; Wang, Q. *Journal of the American Chemical Society* **2010,** 132, (5), 1470-1471.
49. Dong, B.; Li, C.; Chen, G.; Zhang, Y.; Zhang, Y.; Deng, M.; Wang, Q. *Chemistry of Materials* **2013,** 25, (12), 2503-2509.
50. Chen, G.; Ohulchanskyy, T. Y.; Liu, S.; Law, W.-C.; Wu, F.; Swihart, M. T.; Ågren, H.; Prasad, P. N. *ACS Nano* **2012,** 6, (4), 2969-2977.
51. Chen, G.; Ohulchanskyy, T. Y.; Kumar, R.; Ågren, H.; Prasad, P. N. *ACS Nano* **2010,** 4, (6), 3163-3168.
52. Chen, G.; Shen, J.; Ohulchanskyy, T. Y.; Patel, N. J.; Kutikov, A.; Li, Z.; Song, J.; Pandey, R. K.; Ågren, H.; Prasad, P. N.; Han, G. *ACS Nano* **2012,** 6, (9), 8280-8287.
53. Stouwdan, J. W.; Veggel, F. C. J. M. v. *Nano Lett.* **2002,** 2, 733-737.
54. Rocha, U.; Kumar, K. U.; Jacinto, C.; Villa, I.; Sanz-Rodríguez, F.; del Carmen Iglesias de la Cruz, M.; Juarranz, A.; Carrasco, E.; van Veggel, F. C. J. M.; Bovero, E.; Solé, J. G.; Jaque, D. *Small* **2013**.
55. Zhou, J. C.; Yang, Z. L.; Dong, W.; Tang, R. J.; Sun, L. D.; Yan, C. H. *Biomaterials* **2011,** 32, (34), 9059-9067.
56. Fadeel, B.; Garcia-Bennett, A. E. *Advanced Drug Delivery Reviews* **2010,** 62, (3), 362-374.
57. Gautam, A.; van Veggel, F. *Journal of Materials Chemistry B* **2013,** 1, (39), 5186-5200.
58. Boschi, F.; Lo Meo, S.; Rossi, P. L.; Calandrino, R.; Sbarbati, A.; Spinelli, A. E. *Journal of Biomedical Optics* **2011,** 16, (12).

59. Naczynski, D. J.; Tan, M. C.; Zevon, M.; Wall, B.; Kohl, J.; Kulesa, A.; Chen, S.; Roth, C. M.; Riman, R. E.; Moghe, P. V. *Nature Communications* **2013,** 4.
60. Rocha, U.; Jacinto da Silva, C.; Ferreira Silva, W.; Guedes, I.; Benayas, A.; Martínez Maestro, L.; Acosta Elias, M.; Bovero, E.; van Veggel, F. C. J. M.; García Solé, J. A.; Jaque, D. *ACS Nano* **2013,** 7, (2), 1188-1199.
61. Imbusch, B. H. a. G. F., *Optical Spectroscopy of Inorganic Solids*. Oxford Science: New York, 1989.
62. Wang, Y.-F.; Liu, G.-Y.; Sun, L.-D.; Xiao, J.-W.; Zhou, J.-C.; Yan, C.-H. *ACS Nano* **2013,** 7, (8), 7200-7206.
63. Balda, R.; Fernandez, J.; Mendioroz, A.; Adam, J. L.; Boulard, B. *J. Phys.-Condes. Matter* **1994,** 6, (4), 913-924.
64. Serqueira, E. O.; Dantas, N. O.; Monte, A. F. G.; Bell, M. J. V. *J. Non-Cryst. Solids* **2006,** 352, (32-35), 3628-3632.
65. De la Rosa-Cruz, E.; Kumar, G. A.; Diaz-Torres, L. A.; Martinez, A.; Barbosa-Garcia, O. *Optical Materials* **2001,** 18, (3), 321-329.
66. Tanabe, S. *J. Non-Cryst. Solids* **1999,** 259, 1-9.
67. Jaque, D.; Capmany, J.; Luo, Z. D.; Sole, J. G. *J. Phys.-Condes. Matter* **1997,** 9, (44), 9715-9729.
68. Dong, N. N.; Pedroni, M.; Piccinelli, F.; Conti, G.; Sbarbati, A.; Ramirez-Hernandez, J. E.; Maestro, L. M.; Iglesias-de la Cruz, M. C.; Sanz-Rodriguez, F.; Juarranz, A.; Chen, F.; Vetrone, F.; Capobianco, J. A.; Sole, J. G.; Bettinelli, M.; Jaque, D.; Speghini, A. *Acs Nano* **2011,** 5, (11), 8665-8671.
69. Pedroni, M.; Piccinelli, F.; Passuello, T.; Polizzi, S.; Ueda, J.; Haro-Gonzalez, P.; Maestro, L. M.; Jaque, D.; Garcia-Sole, J.; Bettinelli, M.; Speghini, A. *Crystal Growth & Design* **2013,** 13, (11), 4906-4913.
70. Warrier, A. V. R.; Krishnan, R. S. *Naturwissenschaften* **1964,** 51, (1), 8-9.
71. Payne, S. A.; Caird, J. A.; Chase, L. L.; Smith, L. K.; Nielsen, N. D.; Krupke, W. F. *Journal of the Optical Society of America B-Optical Physics* **1991,** 8, (4), 726-740.
72. Krischer, C. *Applied Physics Letters* **1968,** 13, (9), 310-311.
73. Kaminskii, A. A.; Osiko, V. V.; Udovenchik, V. T. *J Appl Spectrosc* **1967,** 6, (1), 23-25.
74. Yang, K.; Zhang, S. A.; Zhang, G. X.; Sun, X. M.; Lee, S. T.; Liu, Z. A. *Nano Letters* **2010,** 10, (9), 3318-3323.
75. Al Faraj, A.; Fauvelle, F.; Luciani, N.; Lacroix, G.; Levy, M.; Cremillieux, Y.; Canet-Soulas, E. *International Journal of Nanomedicine* **2011,** 6, 351-361.
76. Liao, W. Y.; Li, H. J.; Chang, M. Y.; Tang, A. C. L.; Hoffman, A. S.; Hsieh, P. C. H. *Nanoscale* **2013,** 5, (22), 11079-11086.
77. Welsher, K.; Sherlock, S. P.; Dai, H. J. *Proceedings of the National Academy of Sciences of the United States of America* **2011,** 108, (22), 8943-8948.
78. Hirn, S.; Semmler-Behnke, M.; Schleh, C.; Wenk, A.; Lipka, J.; Schaeffler, M.; Takenaka, S.; Moeller, W.; Schmid, G.; Simon, U.; Kreyling, W. G. *European Journal of Pharmaceutics and Biopharmaceutics* **2011,** 77, (3), 407-416.
79. Xiao, K.; Li, Y.; Luo, J.; Lee, J. S.; Xiao, W.; Gonik, A. M.; Agarwal, R. G.; Lam, K. S. *Biomaterials* **2011,** 32, (13), 3435-3446.
80. Balogh, L.; Nigavekar, S. S.; Nair, B. M.; Lesniak, W.; Zhang, C.; Sung, L. Y.; Kariapper, M. S. T.; El-Jawahri, A.; Llanes, M.; Bolton, B.; Mamou, F.; Tan, W.; Hutson, A.; Minc, L.; Khan, M. K. *Nanomedicine: Nanotechnology, Biology and Medicine* **2007,** 3, (4), 281-296.
81. Kumar, R.; Roy, I.; Ohulchanskky, T. Y.; Vathy, L. A.; Bergey, E. J.; Sajjad, M.; Prasad, P. N. *Acs Nano* **2010,** 4, (2), 699-708.
82. Yoshio, T.; Jin, M.; Minfang, Z.; Mei, Y.; Iwao, W.; Sumio, I.; Hiroshi, I.; Masako, Y. *Nanotechnology* **2011,** 22, (26), 265106.
83. Zhang, X. D.; Wu, H. Y.; Wu, D.; Wang, Y. Y.; Chang, J. H.; Zhai, Z. B.; Meng, A. M.; Liu, P. X.; Zhang, L. A.; Fan, F. Y. *International Journal of Nanomedicine* **2010,** 5, 771-781.